Journal of Materials Chemistry A

Accepted Manuscript

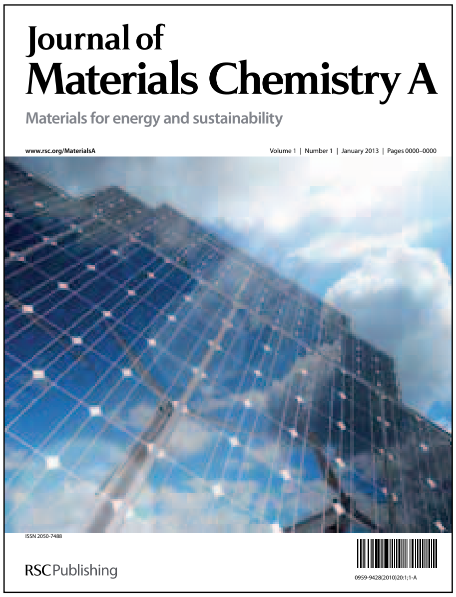

Journal of
Materials Chemistry A
Materials for energy and sustainability
www.rsc.org/MaterialsA
Volume 1 | Number 1 | January 2013 | Pages 0000–0000
ISSN 2050-7488
RSC Publishing

This is an *Accepted Manuscript*, which has been through the RSC Publishing peer review process and has been accepted for publication.

Accepted Manuscripts are published online shortly after acceptance, which is prior to technical editing, formatting and proof reading. This free service from RSC Publishing allows authors to make their results available to the community, in citable form, before publication of the edited article. This *Accepted Manuscript* will be replaced by the edited and formatted *Advance Article* as soon as this is available.

To cite this manuscript please use its permanent Digital Object Identifier (DOI®), which is identical for all formats of publication.

More information about *Accepted Manuscripts* can be found in the **Information for Authors**.

Please note that technical editing may introduce minor changes to the text and/or graphics contained in the manuscript submitted by the author(s) which may alter content, and that the standard **Terms & Conditions** and the **ethical guidelines** that apply to the journal are still applicable. In no event shall the RSC be held responsible for any errors or omissions in these *Accepted Manuscript* manuscripts or any consequences arising from the use of any information contained in them.

Versatile synthesis of high surface area multi-metallic nanosponges allowing control over nanostructure and alloying for catalysis and SERS detection

Shaochun Tang, Sascha Vongehr, Yongguang Wang, Juan Cui, Xiangyu Wang and Xiangkang Meng*

Institute of Materials Engineering, National Laboratory of Solid State Microstructures, and College of Engineering and Applied Sciences, Nanjing University, Jiangsu, P. R. China

Fax: (+86)-25-83595535 E-mail: mengxk@nju.edu.cn.

Abstract

We report a template- and surfactant-free synthesis of multi-metallic nanosponges with controllable composition, porosity, ligament and grain sizes, as well as allowing control over alloying. The inexpensive approach is scalable to industrial production and produces not only sponges of various pure metals such as Ag, Au, Pd, Pt, Co, Ni, Cu, but also bi- and tri-metallic alloys or non-alloys. The synthesis involves fast reduction of metal salts followed by a slow network assembly in ethanol-glycerol mixed solvents shaken in a range of 25-90 ^{o}C. Freeze drying conserves the pores to ensure a high surface area. The involved growth mechanisms are discussed. Tri-metallic alloyed $Ag_{34}Au_{33}Pd_{33}$ sponges with a specific surface area of 96 m^2/g exhibit the highest reported catalytic rate for degradation of azo dyes and 4-nitrophenol reduction. They show higher catalytic activity and better long-term stability for formic acid electro-oxidation compared with Pd-based mono- and bimetallic nanostructures. The excellent catalytic performance is mainly attributed to the high porosity and richness in interfaces. Pressed into discs, the Ag sponges' sensitive SERS activity is highly reproducible over area.

1. Introduction

Metallic sponges with three-dimensional (3D) network nanostructure promise many applications in catalysis,[1-4] sensor technology like bio-molecule detection,[5] water purification,[6] flexible transparent conductors,[7] fuel cells,[8,9] and energy storage devices.[10] Performances for these applications closely depend on low density, high surface area, and high gas permeability, but also enhanced by an reduction of ligament size,[11] high-index facets,[12] combination with other metals,[13] and alloying.[11-14] Thus, synthesis of multi-metallic sponges and control over their nanostructure and alloying is highly desired. However, the most versatile template-based approaches for 3D porous, high surface area metal oxides lack desired results with metals; they fail with noble metals[15] and especially transition metals such as cobalt and nickel. So far, few studies on nanosponges of transition metals and their alloys have been reported.

As for the synthesis of network-like noble metal nanostructures, many methods have been reported including de-alloying,[16,17] pH-controlled glucose reduction,[18] reaction-limited aggregation,[19] and emulsion-based synthesis.[20] These approaches suffer from disadvantages such as requiring many steps, needing charged capping molecules, yielding a low surface area, or from being restricted to few metals. 3D network nanostructures of various metals and alloys were prepared hydrothermally,[2] but surfactants were indispensable and such a method is generally not easily scalable to industrial production. Recently, Krishna *et al.* reported a fast synthesis for Ag, Au, Pd and Pt sponges via rapid reduction of their chlorides by sodium borohydride in aqueous solution.[15] Zhu *et al.* extended this route to noble metallic alloy nanosponges.[21] The method is simple and scalable, but the rapid reaction allows little control especially over multi-metallic systems,[13] such as control over surface area and sizes via temperature or reaction time. In addition, the involved growth mechanisms are difficult to analyze and therefore still unclear, for example, it is impossible to take samples after different times since the reaction is almost immediately finished.

Due to their high surface activity, metal or alloyed nanoparticles (NPs) can fuse into unstable networks during long-term storage at room temperature.[22] Adding inorganic salts or polar solvents with small dielectric constants in aqueous solution facilitates a fusion between charged NPs and can favor a chain-like assembly and production of 2D network-like nanostructures at an oil-water interface.[23-25] Thus, modulation of inter-particle interactions (e.g., van der Waals attraction and electrostatic repulsion) allows to control the assembly of NPs. Multiple metals are desired especially because catalysis can take advantage of metal-metal interactions on the nanoscale, for example via specific interfaces,[26] or synergistic effects.[14,21] However, due to different standard reduction potentials, different metals often nucleate and grow at different times in the wet-chemical synthesis. By using a strong reducer, different metals' precursors can be reduced simultaneously, which is one way to synthesize alloy nanostructures.[21,27,28] A fast nucleation also provides homogeneously sized seeds.[29] The further fusion into a spongy superstructure however allows the more control the slower it proceeds, which also allows investigating the growth mechanism.

Here we report a remarkably simple, template- and surfactant-free, kinetically controlled synthesis of nanosponges with high surface areas suitable for many different metals. One crucial step in gaining more control over the nanostructure is combining the advantages of a fast reduction where the nucleation and growth of NPs occurs, and subsequent slow network assembly and heat-induced fusion. The latter process is performed in ethanol-glycerol mixed solvent shaken in a temperature controlling water bath. Adjusting the preparation temperature T_{prep} and the concentrations of precursor solutions, structural properties like the sizes of ligaments and grains are controlled. A selection of temperature during network assembly (T_{f}) optimizes the surface area. Freeze drying avoids the surface tension that otherwise contracts pores, which has a surprisingly large effect on the BET (Brunauer-Emmett-Teller) surface area. This low-cost process is easily scalable to industrial production. We synthesized Ag, Au, Pt, Pd, Co, Ni, and Cu sponges, as well as Ag-Pd, Ag-Au, Pt-Pd bimetallic and trimetallic alloy sponges with a high specific surface area. Meanwhile non-alloyed bimetallic sponges can be prepared. The alloyed $Ag_{34}Au_{33}Pd_{33}$ sponges exhibit the highest catalytic activity ever reported for degradation of azo dyes and 4-nitrophenol (4-NP) reduction. Also, the performances of these nanosponges for potential applications in formic acid electro-oxidation and surface enhanced Raman scattering (SERS) detection are investigated.

2. Experimental

2.1. Chemicals and materials

Silver nitrate ($AgNO_3$), chlorauric acid ($HAuCl_4$), potassium hexachloroplatinate (IV) (K_2PtCl_6), and potassium chloropalladite (K_2PdCl_4) were provided by Shanghai Jingchun Reagent Co., Ltd. (Aladdin reagent). Nickel (II) chloride hexahydrate ($NiCl_2•6H_2O$), cobalt chloride hexa-hydrate ($CoCl_2•6H_2O$), copper nitrate ($Cu(NO_3)_2•3H_2O$) and hydrazinehydrate ($N_2H_4•H_2O$, 85 wt %) were purchased from Shanghai Chemical Reagent Co. Ltd. 4-nitrophenol (4-NP), rhodamine B (RhB), and sodium borohydride ($NaBH_4$) were obtained from Nanjing chemical Reagent No. 1 Factory. Ammonia aqueous solution (25 wt %), glycerol ($C_3H_8O_3$), smooth silver sheets (purity > 99.8%), and anhydrous ethanol were purchased from the Chemical Reagent Co., Ltd. of National Pharmaceutical Group of China. All materials were of analytic reagent grade and used as received without further purification. Deionized water with resistivity exceeding 18.0 mΩ·cm from a JL-RO 100 Millipore-Q Plus water purifier was used throughout the experiments.

2.2. Synthesis of monometallic nanosponges

In a typical synthesis of silver sponges, 34 mg (0.2 mmol) of $AgNO_3$ was added to 4 mL distilled water with 6 mL glycerol in a 50 mL glass beaker in an ice-water bath (*i.e.* preparation temperature $T_{prep} = 0\ ^oC$), obtaining a clear, colorless $C_{Ag} = 20$ mM $AgNO_3$ solution. During a vigorous stir, 3 mL hydrazine (85 wt%) were added fast. Stirring in ice-water bath continued for another 5 min, during which the mixture turned opaque and gray. Then, under a continuous stir, 7 mL of ethanol was added into the mixed solution (the total volume of the mixed solution is about 20 mL). The resulting suspension was subsequently transferred to a thermostatic oscillator (Shanghai double shun industry development Co., Ltd.) with temperature-during-fusion T_f of 60 ^{o}C. The oscillator shook the mixture at 80 r/min. Gradually, the color of the suspension turned transparent again while a yellowish gray spongy solid gathered to float on the reaction medium after about 2 h. The shaking continued for another 30 min until the solution was colorless (see Fig. 1a). The float was washed five times by shaking with distilled water. The product was freeze-dried for 24 h and a cotton-like solid obtained. Au, Pd, and Pt sponges were synthesized similarly, using instead $HAuCl_4$, K_2PdCl_4, and K_2PtCl_6 at concentrations of C_{Au} = 24 mM, C_{Pd} = C_{Pt} = 12 mM.

For Cu, Ni, and Co, the process was carried out with corresponding metal salts dissolved in 4 mL of ethanol with 6 mL glycerol (leading to C = 10 mM) in a 50 mL glass beaker, all again with vigorous stirring for 20 min in an ice-water bath, during which 4 mL of hydrazine was added dropwise during the first five minutes. The mixture was subsequently microwaved at a power of 800 W for 20 seconds. The mixture turned black due to the formation of metal NPs. The subsequent steps are the same as those for silver.

2.3. Multi-metallic nanosponges

The synthsis is similar, but mixed metal precursor solutions were used instead. The concentrations of presursor metal ions are all 24 mM. Typically, in the synthesis of Ag-Au alloys, a solution consisting of 5 mL $AgNO_3$ and 5 mL $HAuCl_4$

water-glycerol solutions was added to a 50 mL glass beaker suspended in an ice-water bath and stirred for 5 min. As for Ag-Pd, Ag-Pt, Pd-Pt, and Ag-Au-Pd, $AgNO_3$, K_2PdCl_4, and K_2PtCl_6 water-glycerol solutions were used. Different volumes of inidividual water-glycerol solution were selected for alloys with different metal ratios. Molar ratios of noble-metal multi-metallic sponges and corresponding volumes of precursor solutions are shown in Table S1. The procedures are otherwise as above. The alloying is suppressed by a waiting time t_{wait} after fast reducer addition, before which the solutions of the different metals are prepared separately, and after which the preparation is continued with the different metals solutions/suspensions combined.

2.4. Porous discs

The dried nanosponge powders (0.5g for each experiment) were pressed into pellets on a manual powder compressing machine (769YP-100G). The applied mechanical pressures were in a range of 1-10 kN.

2.5. Characterizations

Structure was analyzed by scanning electron microscopy (SEM) with a (Sirion XL, FEI,Hillsboro, OR, USA) at 10 kV accelerating voltage as well as transmission electron microscopy (TEM), selected area electron diffraction (SAED), and high-resolution TEM (HRTEM) on an FEI TECNAI F20 microscope operating at an acceleration voltage of 200 kV. Energy dispersed X-ray spectroscopy (EDS) was performed on the same microscope and an S-3400N II scanning electron microscope (Hitachi company, Japan). The composition and crystallographic properties of the products were investigated by X-ray diffraction (XRD) on a Rigaku Ultima III diffractometer using Cu Kα = 1.5418 Å radiation. X-ray photoelectron spectroscopy (XPS) was performed in a Thermo VG Scientific MultiLab ESCA2000 system with a $CLAM_4$ hemispherical analyzer and at a base pressure below 3×10^{-10} mbar. N_2 adsorption isotherms were measured at 77 K on a Micromeritics ASAP2020 instrument. The specific surface areas and the pore-size distributions were determined using the Brunauer-Emmett-Teller (BET) and the Barrett-Joyner-Halenda (BJH) methods, respectively.

2.6. Catalysis

2.6.1 Degradation of congo red and reduction of 4-nitrophenol

To study catalytic activity, 1.0 mg of dry products was suspended in 2.8 mL aqueous solution of 7.5×10^{-5} M Congo red (5.0×10^{-5} M 4-NP) under constant stirring at r.t. A freshly prepared aqueous solution of $NaBH_4$ (0.20 mL, 1×10^{-1} M) was added. The mixture was immediately transferred into a quartz cuvette with an optical path length of 1 cm, and UV-visible absorption spectra were recorded to monitor changes (Shimadzu UV-3600 UV-vis- NIR spectrophotometer).

2.6.2 Electro-catalysis of formic acid oxidation

Electrochemical measurements were performed on a CHI-660D electrochemical workstation (Chenhua, Shanghai) using a standard three-electrode cell. A platinum foil was used as the counter electrode and a saturated calomel electrode (SCE) as the reference. The working electrode was a glassy carbon electrode (GCE) of 4 mm in diameter (PINE: AFE3T050GC). Prior to surface coating, the GCE was sequentially polished by using 1.0, 0.3 and, 0.05 μm alumina slurry and then washed ultrasonically in water and ethanol for a few minutes. To prepare working electrodes, 5.0 mg of dried products and 100 μL Nafion ethanol solution (5 wt %) were dispersed ultrasonically in 5 mL Millipore water. Then, 5 μL of suspension was drop-cast onto the GCE. Finally, the electrode was dried in an oven at 40 °C for 30 min. Cyclic voltammograms (CVs) were carried out at r.t. in N_2-saturated 0.5 M H_2SO_4 and a solution of 0.5 M H_2SO_4 containing 0.5 M HCOOH at a scan rate of 50 mV s^{-1} in the potential range of -0.1 to 1.0 V (vs SCE). Chronoamperometric tests were carried out at 0.2 V vs SCE in 0.5 M formic acid and 0.5 M H_2SO_4 at r.t. for 1000 s.

2.7. SERS measurements

SERS measurements were recorded with a JY HR800 laser Raman spectrometer at an excitation wavelength of 632 nm (HeNe laser as source). Porous Ag discs made from nanosponges were tested for the sensitivity and reproducibility SERS detection. For this purpose, 2 mL of Rhodamine B (RhB) with different concentrations of 10^{-7}, 10^{-6}, 10^{-5}, and 10^{-4} M was drop casted onto a porous Ag disc. After drying in air, Raman spectra were recorded at room temperature using a 632 nm HeNe laser as source. The characteristic signals for RhB were observed with the porous disc. For a comparison, a bare smooth Ag sheet (purity > 99.8%) was also used as SERS substrate, whereas 10^{-4} M RhB dripped on the smooth Ag sheet could not be detected.

3. Results and discussion

Fig. 1a is a digital photograph of the cotton-like yellowish gray silver products floating on the remnant reaction solution. The floating facilitates separation and thus large scale production. Fig. 1b-c depicts SEM images of the sample from a typical synthesis (C_{Ag} = 20 mM, T_{prep} = 25 °C, T_{f} = 60 °C, and shaking frequency f = 80 rpm). A low-magnification image (Fig. 1b) shows that the products are homogeneously porous. Close observation (Fig. 1c) reveals that they are 3D networks where the network links, also called ligaments, appear necklace-like. The ligaments' diameters as measured across the necklace-beads are (28 ± 8) nm. Fig. 1d shows the corresponding nitrogen adsorption-desorption isotherms. They have a distinct type IV hysteresis, i.e. the pores are mostly in the interior rather than on the surface. The slope of the curves rises significantly above relative pressures of 0.94, indicating that the hysteresis loop can be assigned to mesopores (2-50 nm). The BET specific surface area of the sponges is 39 m^2/g (0.36 m^2□mol^{-1}). This value is larger than the 16 m^2/g for silver nanosponges from rapid reduction,[15] and much higher than the 2 m^2/g achieved by templates.[31,32] BJH pore-size analysis (see inset) indicates a broad range of pores from micropores (< 2 nm) to macropores, which is dominated by pore sizes from 3 to 35 nm. The absence of a plateau at high P/P_0 in the adsorption isotherm implies macropores of diameters larger than 50 nm. If freeze drying is replaced by air drying, the volume is much reduced and the porosity thus changed. Indeed, the SEM analysis confirms that the sample obtained by air drying at room temperature (r.t.) has collapsed pores (Fig. S1a). Air drying at 60 $^{\circ}$C left most pores intact (Fig. S1b), as should be due to the reduced surface tension at elevated temperatures. The BET surface area obtained by air drying at r.t. is only one fourth (9.3 m^2/g) of the freeze dryed sample. A TEM image (Fig. 1e) indicates that the ligaments have a smooth surface. The polycrystalline nature of individual ligaments is indicated by the SAED pattern (inset of Fig. 1c). The HRTEM image (Fig. 1f) shows the interface between two adjacent beads (JCPDS No. 04-0783). The different interplanar spacings of the single-crystalline beads show that the crystals are not aligned. There are four dislocations visible at the interface but no such dislocations in the individual beads.

Similar spongy Au, Pd, and Pt networks were obtained when $HAuCl_4$ (24 mM), K_2PdCl_4 (12 mM), or K_2PtCl_6 (12 mM) were used instead. We will now discuss T_{prep} = 0 °C samples. As shown in a low-magnification SEM image (Fig. S2), the resulting Au networks are also homogeneous over a large area. The diameters of ligaments are narrowly distributed (Fig. 2a). Also Co, Ni, and Cu sponges (Fig. 2d-f) can be obtained with the only difference being that the presursor solutions are microwaved before shaking. Use of excessive reducer prevents oxidation. These materials easily suffer surface oxidation. Drying is necessary for our XRD analysis for example, which is completed sufficiently fast to avoid oxidation. However, since drying can decrease porosity if no freeze drying is available, an exposure to air should anyway be avoided in conceivable commercial applications of these materials, by storing them wet in closed vials with reducers present. The average diameters of ligaments (beads) as estimated from the SEM images are about 21 ± 11, 18 ± 9, 28 ± 12, 33 ± 17, 36 ± 14, and 46 ± 19 nm (a-f respectively). The ligaments in the noble metal sponges, especially those of Ag, Au and Pd, are significantly less beaded than those of the transition metals, which have more distinct necks between the beads. The beads are fused sufficiently that even after 30 min of ultra-sonication (200 W) they still stay together. XRD results for each product (below the respective SEM images) verify the products' high purity and crystallinity (see standard JCPDS numbers in XRD patterns). The peak broadening is associated with the grain size, which is now ($T_{\mathrm{prep}} = 0$ °C) smaller than the bead diameter. According to the Scherrer equation $d = \frac{0.9\lambda}{\beta_{1/2}\cos\theta}$, the grain sizes d are about 12 nm (Au), 4 nm (Pd), 10 nm (Pt), 21 nm (Co), 14 nm (Ni), and 28 nm (Cu). The grain size in Ag sponges obtained at $T_{\mathrm{prep}} = 0$ °C is about 17 nm, smaller than that of Ag product with T_{prep} = r.t. Theses values are all smaller than the bead sizes obtained from SEM, implying that inividual beads are composed of grains.

Heat-induced growth and fusion rates both depend on temperature, so the temperatures for these stages should be adjusted separately in order to gain fine control. The metal salts are reduced by N_2H_4 in below one minute. Aqueous reduction of Pd is autocatalytic and therefore more rapid than with other metals, occurring within seconds. To demonstrate control, we take the especially fast Pd as the most challenging example. The temperature during the preparation of precursor solutions T_{prep} plays an important role for the growth of NPs and determines the sizes of grains in the resultant networks, at times leading to the NPs becoming the single crystalline beads in the final products. Fig. 3 shows TEM images of Pd networks from different T_{prep} while keeping other parameters. The dark spots in the 2D TEM projection are due to overlapping network links. The Pd networks obtained at T_{prep} = 0, 25, and 60

^{o}C look globally much the same (compare Fig. 3a, c, and e), but their beads have different diameters (about 18, 35 and 48 nm, respectively). Those from 60 ^{o}C have smoother necks between beads. The diffraction rings (insets) recorded from individual ligaments correspond to various facets of face-centered cubic (fcc) Pd, and reveals that an individual ligament is polycrystalline. The SAED patterns also imply different grain sizes, and this is further confirmed by HRTEM. The T_{prep} = 0 ^{o}C sample's beads consist of (4.5 ± 2) nm diameter grains (Fig. 3b), consistent with XRD. Average grain size increases to (8.2 ± 4) nm when T_{prep} is r.t. (Fig. 3d), and to (17.5 ± 5) nm for 60 ^{o}C (Fig. 3f). According to the diffraction peaks in XRD patterns (Fig. S3), and grain sizes from different T_{prep} of 0 ^{o}C, 25 ^{o}C and 60 ^{o}C are about 5 nm, 8 nm, and 13 nm, consistent with HRTEM results.

The temperature during the subsequent fusion T_{f} is especially important for the pore size; a temperature of T_{f} = 60 ^{o}C produces the highest surface areas. For example, the surface areas of Pd sponges obtained with T_{f} of r.t., 50, 60, 80, and 90 ^{o}C are 21, 40, 47, 31, and 33 m^2/g, respectively. It is worth noting that concentrations below 2 mM and above 50 mM do not obtain sponges. Lower concentrations lead to an insufficient number density of NPs, which do not find each other in time to aggregate. The large NPs formed at high concentrations form dense particle aggregates. When temperatures were as before (T_{prep} = 0 ^{o}C and T_{f} = 60 ^{o}C), varying the $PdCl_6^{2-}$ concentration C_{Pd} obtains average bead diameters in the range of 5 to 85 nm, as shown in Fig. S4a-d. For example, when C_{Pd} was 50 mM, the products diameters are (63 ± 21) nm (Fig. S4d). The necks between the beads look quite narrow, thus little growth occurred after fusion. The SAED pattern recorded from one bead (the inset) reveals that the beads are polycrystalline and the grains have their crystallographic orientations in random directions. The reaction parameters and corresponding grain and bead sizes and BET surface areas for all the Pd products are listed in Table 1. The BET surface area is optimized around 12 mM.

In order to study the shape evolution over time, we collected intermediate Pd products after different shaking times t_{shake} of 0, 5, 30, 60, 120, and 150 min with C_{Pd} $=22.5$ mM, $T_{\text{prep}} = 0^{\circ}$C and $T_{\text{f}} = 60^{\circ}$C. Before adding ethanol ($t_{\text{shake}} = 0$ min), NPs with diameter below 10 nm were obtained (Fig. S5a). HRTEM image (the inset) indicates that they are single-crystalline and their diameters are (4 ± 2) nm. After adding ethanol and shaking for 1 min, NPs aggregated as demonstrated by the HRTEM image in Fig. S5b. After shaking for 5 min, near-spherical NPs with diameters of 11-15 nm formed (Fig. S5c). With $t_{\text{shake}} = 30$ min, larger NPs of 22-25 nm are obtained and some of them combined into short chains (Fig. S5d). After 60 min, networks are obtained (Fig. S5e). Their diameters are not uniform, which is further confirmed by TEM (see inset). When shaking continues for 120 min, the beads have grown to an average of ~35 nm in diameter (Fig. S5f). The time-dependent shape evolution indicates that NPs fuse into beads which fuse to each other resulting in short chains, while the beads still grow. Adjacent beads and short chains attach in random directions, resulting in the formation of 3D structure.[22] Fig. S6a is a higher-magnification TEM image of the neck between two adjacent beads in the t_{shake} = 60 min sample (as shown in Fig. S5e). HRTEM images (Fig. S6b) recorded from inside the selected dashed frame reveals twins and dislocations at the interface. The many dislocations and twins at the interface may be due to the bending at the necks[33] when larger structures slightly deform during the continued shaking.

Using solutions containing two kinds of metal ions obtains again spongy floating products. Fig. 4 shows the product from a mixed solution of K_2PdCl_4 and $AgNO_3$ with a molar ratio $r = n_{\mathrm{Pd}}/n_{\mathrm{Ag}}$ of 1.0 (defined as $Ag_{50}Pd_{50}$). A large volume difference due to different methods of drying is observed again (Fig. 4a). The freeze dryed sample's porosity seems completely preserved. SEM (Fig. 4b-c) reveals that the ligaments are again composed of fused beads with relatively thick necks between them, as seen before with the pure noble metals. The beads' diameters are (45 ± 11) nm. SEM elemental mapping (Fig. 4d) already indicates a well-mixed distribution of the two metals. HRTEM (Fig. 4e) reveals the grains in the beads with their different lattice spacings. The inter-planar distances are measured to be 0.231 and 0.205 nm, which falls between those of Ag (111) and Pd (111). The XRD pattern (Fig. 4f) has the peaks situated between the corresponding Ag and Pd reference peaks. On the basis of the XRD data, the lattice constant is 0.3921 nm, which is between those of Ag and Pd (a_{Ag} = 0.4086 nm, a_{Pd} = 0.3890 nm), showing the sample is Ag-Pd alloy.[21] It is observed from a magnified XRD pattern (Fig. 4g) that the diffraction peaks shift toward the Pd reference with an increase of r, indicating that composition modulation is achieved by varying r without destroying the alloying.

The method is extended to bimetals such as Ag-Au, Ag-Pt, Pd-Pt, and Co-Ni. Their corresponding XRD patterns are shown in Fig. S7a-d. Peak broadening due to alloying is especially visible for the Ag-Pt sponges. Metal-metal molar ratios are adjusted via the volume ratio of metal ion solutions. We obtained sponges with different Ag/Pd (Fig. 4f-g) and Ag/Au (Fig. S7a) ratios; none of the ratios impacts the alloying. Aside from such bimetallic structures, various trimetallic alloy sponges, such as Ag-Au-Pt, Ag-Pd-Pt and Ag-Au-Pd were also synthesized. The molar compositions are summarized in Table S1. Fig. 5a-b shows typical $Ag_{34}Au_{33}Pd_{33}$ sponges with bead diameters around 18-25 nm. They have a specific surface area of 96 m^2/g. This is the highest BET value reported so far for any multi-metallic nanostructures from template-free methods. In the XRD pattern (Fig. 5c), there are four diffraction peaks corresponding to (111), (200), (220), and (311) planes of the fcc structure. The diffraction peaks are between monometallic Ag and Pd. Compared with the XPS spectrum of monometallic Ag sponges, a slight shift of the Ag 3*d* peak was observed for the trimetallic $Ag_{34}Au_{33}Pd_{33}$ sponges (Fig. 5d), implying a change in the electronic structure of Ag when it is alloyed.[34]

The preparation after the reducer has been added and before shaking in water bath takes about 5 minutes. During continuous stirring for the 5 minutes, nucleation is already completed and growth of NPs is well under way in case of the noble metals. Performing this procedure with the different metals' precursors separated, we may combine them into one vessel at any time after adding the reducer, say after t_{wait} in a range of 0 to 5 minutes, and then go on with the preparation just as before, namely with a single mixed solution containing all metals together. The longer one waits before combining the metals, the less the products can be alloyed. For example, preparing Ag and Pd separately for t_{wait} = 5 minutes and thus combining NPs' suspensions, the XRD pattern (Fig. S8) shows that the sponges are not alloys but a mixture of Ag and Pd NPs instead. The Ag and Pd peaks did not shift relative to their reference peaks. Also, preparing Ag-Pd networks in order to analyze the timing more systematically revealed that the peaks are already shifted after only t_{wait} = 1 min (data not shown). In order to further control alloying, we will use different waiting times (0-5 min) in future work. HRTEM could classify alloying degrees at waiting times above one minute by the average size of the different metals' domains, i.e. whether the grains or perhaps whole beads are predominantly one of the involved metals. This analysis combined with catalytic tests of the products could reveal the difference between atomic scale alloying and metal-metal domain interfaces in catalysis.

In order to further reveal the formation mechanisms, we performed a series of control experiments. With water replacing ethanol, there are no nanochains or networks but only separated NPs (Fig. S9a). This is due to the electrostatic repulsion between metal NPs in aqueous solution.[24,25] The weak polarity ethanol suppresses dipole layers[25,35] so that the NPs collide and assembly in some directions. The glycerol's viscosity slows the movement of NPs and thus their aggregation, which facilitates the formation of chains. If the glycerol is replaced by water, dense particle aggregates form (Fig. S9b). Vibration is important for bringing larger particles together so that they can fuse. A vibration frequency of f = 80 r/min is most suitable for the formation of homogeneous porosity. This value being optimal is similar to the issue about that T_{f} = 60 $^{\mathrm{o}}$C gives the largest surface area, namely the responsible mechanisms likely combine many involved factors. For example, a higher T_f works somewhat like the ethanol, because it reduces the dipole layers directly and helps overcome the hurdle those layers pose to attachment. Thus, conceivably, beads are immediately attached to the network on first contact, and thus do not wander around to find energetically more favorable positions deeper inside the already grown network. This predicts higher specific surface area with higher T_f. On the other hand, if T_f becomes too high, it may act similar to strong vibration in that it allows the already attached beads and short chains to move and bend inwards, thereby lowering surface area. Optimal combinations of such parameters as vibration frequency f and T_f are thus difficult to predict quantitatively and must be found by trial and error.

The preparation stage is a coordination-then-reduction for Cu and Ni, which involves microwaving. Also, the single-crystalline Ag beads (Ag sponges shown as Fig. 1) discussed in the very beginning contrast with the polycrystalline Pd beads discussed (Fig. 3) after that, so the growth mechanisms obviously differ between the different products. However, a typical formation process can be presented as follows (see scheme 1): N_2H_4 reducer is added in excess to avoid oxidation and reduce rapidly, thus all precursor ions are reduced instantaneously. Stirring at low T, formed nuclei grow relatively slowly into NPs, which fuse due to the high surface energy in the absence of surfactants. The NPs have negative surface charges in solution[25] which hinders fusion. As discussed, the addition of ethanol mitigates this problem. The fusion of the NPs leads to larger particles that will later serve as the beads in the chain-like network links. When the ethanol to water ratio is high, the beads have larger diameters, which confirms once more that the ethanol mainly facilitates the fusion of NPs into the beads. When the mixture is shaken, the beads collide and assemble into small chains and start the 3D network structure. Shorter shaking times result in pronounced necks. If given more time, the necks further growth by attaching more NPs at a constant temperature, resulting in a smoother appearance of the network links.[30] That NPs are still added means that the separation into preparation and shaking stages does not divide neatly between growth stages such as NPs-to-bead versus bead-to-network formation. Since the late time thickening can be enhanced by higher temperatures (comparing Fig. 3c with 3e), some Ostwald ripening may be involved in the heat-induced fusion process, too.

Especially considering catalytic applications, recent results have impressively confirmed the advantages of porous metal[29,36] and multi-metal nanostructures.[37,38] We investigate the potential of our materials for catalytic applications by analyzing three benchmark reactions: degradation of azo dyes, reduction of 4-NP, and formic acid electro-oxidation. As a representative case, the catalytic activity was first investigated in the decolourization of Congo red, a kind of azo dye with two -N=N- bonds. When the $Ag_{34}Au_{33}Pd_{33}$ sponge was added, the color faded visibly in minutes. The maximum absorption band, being centered at 493 nm, is assigned to the conjugated system formed by the -N=N- bonds of Congo red and used to monitor the bleaching.[39] After addition of the $Ag_{34}Au_{33}Pd_{33}$ sponges, the absorption at 493 nm disappears along with the breakage of the -N=N- bonds (Fig. 6a). The concentration of BH_4^- ions is much higher than that of Congo red and remains basically constant during the reaction. Therefore, the catalytic rates can be calculated via pseudo-first-order kinetics.[40] The rate constant k is determined from the plot of $\ln A_{493nm}$ (A_{493nm} being the absorbance at 493 nm) vs. reduction time (Fig. 6b). The sponges can be reused after washing and freeze drying, and have not been found significantly poisoned during the second and third trials. The rate constant of 74.8×10^{-3} s^{-1} for the $Ag_{34}Au_{33}Pd_{33}$ sponge is higher than those for the same mass of Pd sponges (2.56×10^{-3} s^{-1}), and $Ag_{50}Pd_{50}$ sponges (14.5×10^{-3} s^{-1}). The activity of the $Ag_{34}Au_{33}Pd_{33}$ is two times more than that of 4 nm Pd NPs (36.1×10^{-3} s^{-1}).[39] Without addition of catalysts, the bleaching of Congo red proceeds slowly even in $NaBH_4$, and its reaction rate constant is 2.19×10^{-5} s^{-1}. The decolourization of Congo red is accelerated with the increase in reaction rate constant by more than 10^3 times. Reduction of 4-NP proceeded rapidly when the $Ag_{34}Au_{33}Pd_{33}$ was added as seen from the bleaching of the solution during about 40 seconds. Fig. 6c depicts the UV-vis absorption peak at 400 nm after different times. The rate constant k is determined similarly from the plot of $\ln A_{400nm}$ vs. reduction time (Fig. 6d). In the presence of 5 nm Pd NPs, and Pd, $Ag_{50}Pd_{50}$, and $Ag_{34}Au_{33}Pd_{33}$ sponges, k is 11.2×10^{-3} s^{-1}, 2.3×10^{-3} s^{-1}, 6.6×10^{-3} s^{-1}, and 41.8×10^{-3} s^{-1}, respectively. The catalytic activity of $Ag_{34}Au_{33}Pd_{33}$ is about 4 times stronger than pure Pd NPs, and about 15 times faster than Pd sponges. The $Ag_{34}Au_{33}Pd_{33}$ sponges exhibit the highest reported catalytic rate for degradation of azo dyes and 4-NP reduction.

Pd-based catalysts are attractive for direct formic acid fuel cells. Fig. 7a shows the cyclic voltammograms (CVs) of glass-carbon electrodes (GCE) modified again with the mentioned four materials in N_2-saturated 0.5 M H_2SO_4 solution at a scan rate of 50 mV s^{-1}. The metal mass loading ρ on the electrode (in mg cm^{-2}) is the same for all materials. The peaks appearing between 0-0.4 V (vs. SCE) originates from desorption of atomic hydrogen. The electrochemically active surface area (EASA) of the GCEs was determined by the charge under the hydrogen desorption peak.[41] The specific EASAs are Q_H / (ρ × 0.21 mC cm^{-2}),[41] where Q_H is the columbic charge surface density for hydrogen desorption, and 0.21 mC cm^{-2} is the charge required for the adsorption of a H_2 monolayer on a smooth surface. The specific EASA of the $Ag_{34}Au_{33}Pd_{33}$ alloy sponges is 87.6 m^2g^{-1} (inset of Fig. 7a), which is significantly higher than that of pure Pd NPs (19.1 m^2g^{-1}), Pd sponges (37.2 m^2g^{-1}), and $Ag_{50}Pd_{50}$ sponges (47.6 m^2g^{-1}). The sponges are electrochemically more accessible, which is very important for electro-catalysis. Good electronic conduction through the solid ligaments combined with an increase of the active area accessible to the reactant molecules due to easy passage of ions through the pores is important for electrochemical reactions.

Fig. 7b shows CVs of the GCEs in a N_2-saturated 0.5 M H_2SO_4 solution containing 0.5 M formic acid. All the materials show similar formic acid electro-oxidation current peaks in the forward scan and another peak in the reverse scan due to the removal of intermediate species (CO) formed in the forward scan. All samples exhibited a weak peak related to hydrogen oxidation below 0.1 V. There are two obvious peaks for the formic acid oxidation, occurring at 0.65 V in the forward scan and 0.32 V in the reverse scan. The forward and reverse anodic peak currents of

$Ag_{34}Au_{33}Pd_{33}$ are considerably higher than those of Pd and $Ag_{50}Pd_{50}$ sponges, in agreement with the ECSAs. The peak potential of the formic acid oxidation for the Pd sponge electrode is about 0.35 V and the corresponding peak current density is 0.61 A mg^{-1}. When the Ag is alloyed into the Pd sponges, the onset oxidation potential obviously shifted negatively (about 0.07 V shift), and the corresponding mass current density greatly increased to 0.84 A mg^{-1}. The mass current density at 0.28 V for the $Ag_{34}Au_{33}Pd_{33}$ sponge electrode is as high as 1.02 A mg^{-1}, about 4 times higher than those of the Pd NPs (0.28 A mg^{-1}), and about two times that of the Pd sponges. A similar phenomenon was also observed for trimetallic alloyed nanospheres,[42] nanowires,[11] and sponges[21] for formic acid oxidation. The $Ag_{34}Au_{33}Pd_{33}$ sponges are superior due to the synergy that can be provided by three different metals,[34] including alloying effects,[14,21] grain-grain interfaces,[43] as well as Pd's hydrogen absorption capability.[44] The higher activity can be attributed to three combining factors: (1) high surface area of the network results in a higher ECSA; (2) the porous networks provide both, electronic and ionic mobility; (3) the multi-metallic nature (alloying, metal-metal interfaces) provides especially many active sites.

To measure the long term stability of the materials, current-time responses were monitored at a fixed potential of 0.2 V for a duration of 1000 s in N_2-saturated mixed solution containing 0.5 M H_2SO_4 and 0.5 M HCOOH. Typical results are shown in Fig. 7c. The $Ag_{34}Au_{33}Pd_{33}$ exhibits the highest initial current, likely because it has the largest number of active sites and thus more adsorbed formic acid and formate initially available. Though all electrodes display an initial fast current decay followed by a slower attenuation, the current at the GCE modified with sponges decays slower than with the Pd NPs. This may be due to effective removal of the initially adsorbed intermediate species (CO), consistent with the CV measurements. The oxidation current of the $Ag_{34}Au_{33}Pd_{33}$/GCE after 1000 s still remains to be the highest. The Ag-Au-Pd electrode has a better tolerance towards poisoning by CO-like intermediates and long-term stable activity under continuous operating conditions. There is little change in the CVs of the $Ag_{34}Au_{33}Pd_{33}$ before and after the stability test, which illustrates once more that these sponges are stable electrocatalysts. There is no visible morphology change in the sponges after the stability test. The results indicate that the alloying leads to very excellent CO tolerance ability.[45] The Ag-Au-Pd sponges can be thus used as advanced catalysts in direct formic acid fuel cells.

Developing metallic substrates for SERS has broad applications in trace-amount chemical analyses. SERS substrates having a high sensitivity combined with reproducibility are highly desirable. 3D structures can enhance SERS by electromagnetic amplification in pores. Gold and silver sponges show broad surface plasmon absorptions in the visible and IR; their SERS is not restricted to only few excitation wavelengths, as is the case for NPs with particular sizes. Because freeze drying prevents the contraction of pores and thus also removes solvents more thoroughly, the nanosponges can be pressed into pellets. This does not lower the BET surface area. Fig. 8a is a photograph of a 1.2 cm diameter disc of Ag made with a pressure of 10 kN applied to Ag sponges as shown in Fig. 1. The SEM (Fig. 8b) reveals that the disc's surface is homogeneously porous. Fig. 8c shows SERS spectra measured from Rhodamine B (RhB) of different concentrations between 10^{-7} to 10^{-4} M dripped on a porous Ag disc. Even 10^{-7} M is still distinguishable from noise, indicating that the SERS activity is higher than that of SERS substrates using colloidal Ag NPs,[46] 2D silver dendrites,[47] Ag-Au bimetallic dendrites,[48] and reported in recent studies of similar spongy mono- and bi-metallic substrates.[13,15] We measured Raman signals at this limit concentration for ten randomly chosen spots. The standard deviation in peak intensities is 5.1%. Such reproducibility is higher than that of common SERS substrates using Ag NPs that must be located close each other with respect to SERS "hot spots" to obtain a large enhancement,[46] and comparable to Ag replicas of butterfly scales.[49] The high SERS sensitivity and reproducibility are due to the uniform surface porosity of the Ag discs in 3D spatial resulting in abundant and uniformly distributed SERS hot spots, which promises direct applications as nanodevices for SERS detection.

4. Conclusions

We have developed a versatile preparation of 3D metal networks from pure metals (Ag, Au, Co, Cu, Ni, Pd, and Pt) and their bi- and tri-metals. The method is applicable to noble and transition metals. In addition to controlling the mixed solvent's viscosity and dipole character, precursor concentrations and suchlike, the growth can be especially well controlled because the initial and subsequent growth stages are separated and performed under different conditions, including different modes of agitation. The tri-metallic $Ag_{34}Au_{33}Pd_{33}$ sponges exhibit the highest reported catalytic rate for the degradation of azo dyes and 4-NP reduction, promising applications in the treatment of wastewater. Additionally, they show better catalytic activity and long-term stability for formic acid electro-oxidation than Pd-based mono- and bimetallic sponges. Porous Ag discs made from Ag sponges show a high SERS activity which is uniform over area, allowing good reproducibility.

This work provides a general strategy for 3D nanostructured networks from a wide variety of metals and can be extended to other multi-metallic systems for magnetic, optical, and catalytic applications. Much future research can revolve around the properties of the transition metal sponges and further controlling structure and metal ratios for example in order to optimize catalytic strength. As discussed, the most promising future work may be further analysis of and control over the degree of alloying which the separation of reaction steps allowed us to achieve already.

Acknowledgments

This work was jointly supported by the PAPD, the Fundamental Research Funds for the Central Universities, the Natural Science Foundation of Jiangsu Province, the National Natural Science Foundation of China, and the State Key Program for Basic Research of China.

References:

1. J. T. Zhang and C. M. Li, *Chem. Soc. Rev.*, 2012, **41**, 7016.
2. J. H. Cui, H. Zhang, Y. F. Yu, Y. Liu, Y. L. Tian and B. Zhang, *J. Mater. Chem.*, 2012, **22**, 349.
3. L. Ye, Y. Wang, X. Y. Chen, B. Yue, S. C. Tsang and H. He, *Chem. Commun.*, 2011, **47**, 7389.
4. Y. Xu, R. Xu, J. H. Cui, Y. Liu and B. Zhang, *Chem. Commun.*, 2012, **48**, 3881.
5. X. Y. Lang, H. Y. Fu, C. Hou, G. F. Han, P. Yang, Y. B. Liu and Q. Jiang, *Nat. Commun.*, 2013, **4**, 2169.
6. M. Arkas, L. Eleades, C. M. Paleos and D. Tsiourvas, *J. Appl. Polym. Sci.*, 2005, **97**, 2299.
7. X. Y. Zeng, Q. K. Zhang, R. M. Yu and C. Z. Lu, *Adv. Mater.*, 2010, **22**, 4484.
8. B. C. H. Steele and A. Heinzel, *Nature*, 2001, **414**, 345.
9. Y. Ding, M. Chen and J. Erlebacher, *J. Am. Chem. Soc.*, 2004, **126**, 6876.
10. F. H. Meng and Y. Ding, *Adv. Mater.*, 2011, **23**, 4098.
11. C. Z. Zhu, S. J. Guo and S. J. Dong, *J. Mater. Chem.*, 2012, **22**, 14851.
12. L. Zhang, J. W. Zhang, Q. Kuang, S. F. Xie, Z. Y. Jiang, Z. X. Xie and L. S. Zheng, *J. Am. Chem. Soc.*, 2011, **133**, 17114.
13. H. Y. Liu and Q. Yang, *J. Mater. Chem.*, 2011, **21**, 11961.
14. Y. Xu, Y. Q. Yuan, A. J. Ma, X. Wu, Y. Liu and B. Zhang, *Chemphyschem*, 2012, **13**, 2601.
15. K. S. Krishna, C. S. S. Sandeep, R. Philip and M. Eswaramoorthy, *ACS Nano*,

2010, **4**, 2681.

16. J. Erlebacher, M. J. Aziz, A. Karma, N. Dimitrov and K. Sieradzki, *Nature*, 2001, **410**, 450.
17. Y. Ding and J. Erlebacher, *J. Am. Chem. Soc.*, 2003, **125**, 7772.
18. G. W. Qin, J. Liu, T. Balaji, X. Xu, H. Matsunaga, Y. Hakuta, L. Zuo and P. Raveendran, *J. Phys. Chem. C*, 2008, **112**, 10352.
19. B. Vishwanath, S. Patra, N. Munichandraiah and N. Ravishankar, *Langmuir*, 2009, **25**, 3115.
20. Y. Song, R. M. Garcia, R. M. Dorin, H. Wang, Y. Qiu, E. N. Coker, W. A. Steen, J. E. Miller and J. A. Shelnutt, *Nano Lett.*, 2007, **7**, 3650.
21. C. Z. Zhu, S. J. Guo and S. J. Dong, *Chem. Eur. J.*, 2013, **19**, 1104.
22. H. B. Xia and D. Y. Wang, *Adv. Mater.*, 2008, **20**, 4253.
23. H. Zhang and D. Y. Wang, *Angew. Chem. Int. Ed.*, 2008, **47**, 3984.
24. R. K. Joshi and J. J. Schneider, *Chem. Soc. Rev.*, 2012, **41**, 5285.
25. J. P. Xie, Q. B. Zhang, J. Y. Lee and D. I. C. Wang, *J. Phys. Chem. C Lett.*, 2007, **111**, 17158.
26. S. C. Tang, S. Vongehr, G. R. He, L. Chen and X. K. Meng, *J. Colloid Interf. Sci.*, 2012, **375**, 125.
27. Y. Xu, S. Hou, Y. Liu, Y. Zhang, H. Wang and B. Zhang, *Chem. Commun.*, 2012, **48**, 2665.
28. J. Chai, F. Li, Y. Hu, Q. Zhang and L. Niu, *J. Mater. Chem.*, 2011, **21**, 17922.
29. S. C. Tang, S. Vongehr, Z. Zheng, H. Ren and X. K. Meng, *Nanotechnology*, 2012,

23, 255606.

30. M. H. Wang, Y. J. Li, Z. X. Xie, C. Liu and E. S. Yeung, *Mater. Chem. Phys.*, 2010, **119**, 153.
31. D. Walsh, L. Arcelli, T. Ikoma, J. Tanaka and S. Mann, *Nat. Mater.*, 2003, **2**, 386.
32. J. He, T. Kunitake and T. Watanabe, *Chem. Commun.*, 2005, 795.
33. S. C. Tang, S. Vongehr and X. K. Meng, *Chem. Phys. Lett.*, 2009, **477**, 179.
34. S. Zhang, S. J. Guo, H. Y. Zhu, D. Su and S. H. Sun, *J. Am. Chem. Soc.*, 2012, **134**, 5060.
35. H. X. Wu, H. Li, Y. J. Zhai, X. L. Xu and Y. D. Jin, *Adv. Mater.*, 2012, **24**, 1594.
36. H. H. Wang, Z. H. Sun, Y. Yang and D. S. Su, *Nanoscale*, 2013, **5**, 139.
37. L. Wang and Y. Yamauchi, *J. Am. Chem. Soc.*, 2010, **132**, 13636.
38. F. Wang, C. H. Li, L. D. Sun, C. H. Xu, J. F. Wang, J. C. Yu, C. H. Yan, *Angew. Chem. Int. Ed.*, 2012, **51**, 4872.
39. L. Xu, X. C. Wu and J. J. Zhu, *Nanotechnology*, 2008, **19**, 305603.
40. S. C. Tang, S. Vongehr and X. K. Meng, *J. Phys. Chem. C*, 2010, **114**, 977.
41. N. Tian, Z. Y. Zhou, S. G. Sun, Y. Ding and Z. L. Wang, *Science*, 2007, **316**, 732.
42. G. T. Fu, W. Han, L. F. Yao, J. Lin, S. H. Wei, Y. Chen, Y. W. Tang, Y. M. Zhou, T. H. Lu and X. H. Xia, *J. Mater. Chem.*, 2012, **22**, 17604.
43. S. J. Guo, S. J. Dong and E. K. Wang, *ACS Nano*, 2010, **4**, 547.
44. S. Kishore, J. A. Nelson and P. C. Eklund, *J. Alloys Compd.*, 2005, **389**, 234.
45. L. Zhang, J. W. Zhang, Z. Y. Jiang, S. F. Xie, M. S. Jin, X. G. Han, Q. Kuang, Z. X. Xie and L. S. Zheng, *J. Mater. Chem.*, 2011, **21**, 9620.

46. C. Y. Jiang, S. Markutsya and V. V. Tsukruk, *Langmuir*, 2004, **20**, 882.

47. Z. Zheng, S. C. Tang and X. K. Meng, *Mater. Chem. Phys.*, 2011, **129**, 594.

48. S. C. Tang, S. Vongehr and X. K. Meng, *J. Mater. Chem.,* 2010, **20**, 5436.

49. Y. W. Tan, X. N. Zang, J. J. Gu, D. X. Liu, S. M. Zhu, H. L. Su, C. L. Feng, Q. L. Liu, W. M. Lau, W. J. Moon and D. Zhang, *Langmuir*, 2011, **27**, 11742.

Figure captions

Table 1 Summary of reaction parameters and corresponding properties of Pd products

Fig. 1. Digital photograph showing spongy silver products floating on the reaction solution (a). SEM (b-c), nitrogen adsorption-desorption isotherm (d) with pore-size distribution curve (inset), TEM (e) and HRTEM (f) images of typical silver sponges obtained with C_{Ag} = 20 mM, T_{prep}= r.t., T_{f} = 60 °C, and f = 80 rpm. The inset of c is SAED pattern recorded from one bead in an individual ligament of the Ag sponges.

Fig. 2. SEM images of Au, Pd, Pt, Co, Ni, and Cu sponges (a-f, respectively). The corresponding XRD patterns are always below the images. The seven kinds of metals (including Ag) are close in the periodic table. Concentrations C of the different metal ion solutions are 24, 12, 12, 10, 10, and 15 mM for (a-f) respectively.

Fig. 3. TEM and HRTEM images of the Pd sponges obtained at different T_{prep} of 0 $^{\mathrm{o}}$C (a, b), r.t. (c, d), and 60 $^{\mathrm{o}}$C (e, f) while other conditions remained (C_{Pd} = 12 mM, T_{f} = 60 °C, and f = 80 rpm). The SAED patterns in the insets are recorded from a ligament in the corresponding samples.

Fig. 4. Digital photographs (a) showing the Ag-Pd products from air drying at r.t. (on the left), air drying at 60 $^{\mathrm{o}}$C (middle), and freeze drying (right). SEM image (b, c), EDS-mapping (d), and HRTEM (e) images of the $Ag_{0.5}Pd_{0.5}$ alloy sponges. XRD patterns (f) of Ag-Pd sponges obtained with different molar ratios between $PdCl_4^-$ and Ag^+ ions. The (111) and (200) diffraction peaks are between the corresponding peaks of Ag and Pd (g), showing the samples are Ag-Pd alloy.

Fig. 5. SEM images (a, b), XRD pattern (c), and high resolution XPS spectrum of the Ag 3*d* peak (d) of the $Ag_{34}Au_{33}Pd_{33}$ and the Ag sponges. The inset of c is a magnification of the (111) and (200) diffraction peaks.

Scheme 1. Schematic illustration of the formation of nanosponges with 3D network-like nanostructure in ethanol-glycerol mixed solutions.

Fig. 6. UV-Vis absorption spectra for the decolourization of Congo red (a) and 4-NP reduction (c) in the presence of $Ag_{34}Au_{33}Pd_{33}$ nanosponges. The plot of ln$A$ versus time for the corresponding reactions (b and d). A is the absorption intensity.

Fig. 7. CVs of Pd NPs, Pd, $Ag_{50}Pd_{50}$, and $Ag_{34}Au_{33}Pd_{33}$ sponges modified GCs in a N_2-saturated 0.5 M H_2SO_4 (a) and mixed solution containing 0.5 M H_2SO_4 and 0.5 M HCOOH (b) at 50 mV/s. Chronoamperometry responses (c) were monitored at a fixed potential of 0.2 V versus SCE in the same mixed solution.

Fig. 8. Photograph of a disc made by applying a pressure of 10 kN on silver nanosponges. SEM image (b) showing a magnification of surface morphology of the disc. Raman spectra (c) of 10^{-4} M RhB on a smooth Ag sheet (light yellow curve), and RhB with different concentrations from 10^{-4} M to 10^{-7} M on the porous Ag disc.

Table 1 Summary of reaction parameters and corresponding properties of Pd products

C_{Pd} /mM	T_{prep} /$^{\mathrm{o}}$C	T_{f} /$^{\mathrm{o}}$C	d_{bead} /nm	Grain size *d* /nm	Dominant BJH pore sizes/ nm	BET surface area/ m^2 g^{-1}
12	0	60	18±9	4.5 ± 2	14～52	47
12	25	60	35±12	8.2 ± 4	/	/
12	60	60	48±16	17.5 ± 5	/	/
12	0	25	19±10	4.3 ± 2	4～48	21
12	0	90	51±21	21.2 ± 8	2～60	33
2	0	60	7±2	4.5±1	9～25	18
4	0	60	17±6	9.0±3	15～37	29
8	0	60	20±11	8.6±4	11～44	34
24	0	60	35 ± 12	15.4±9	11～38	22
50	0	60	63±21	22.5±14	10～23	14

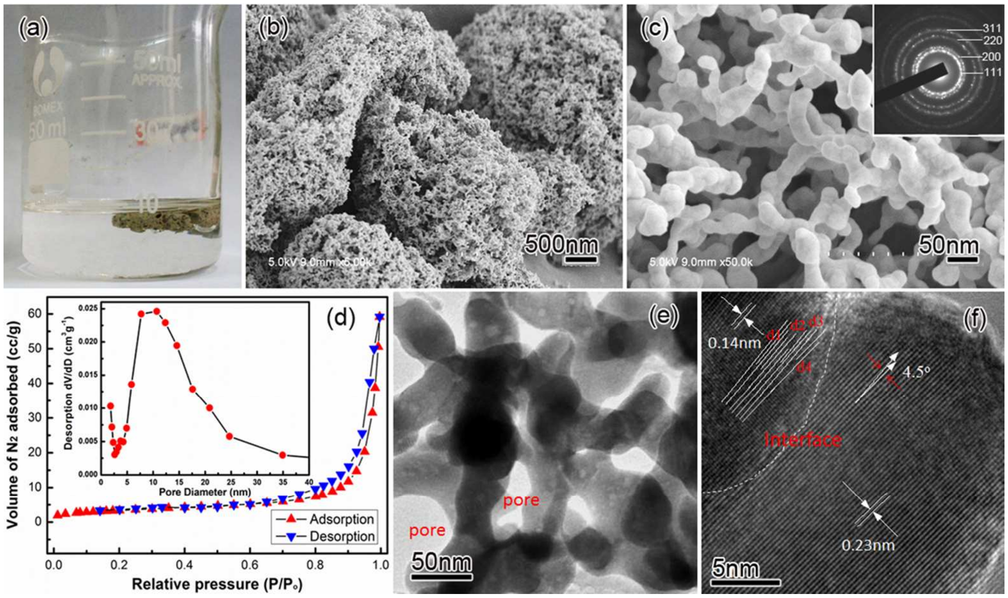

Fig. 1. Digital photograph showing spongy silver products floating on the reaction solution (a). SEM (b-c), nitrogen adsorption-desorption isotherm (d) with pore-size distribution curve (inset), TEM (e) and HRTEM (f) images of typical silver sponges obtained with CAg = 20 mM, Tprep= r.t., Tf = 60 °C, and f = 80 rpm. The inset of c is SAED pattern recorded from one bead in an individual ligament of the Ag sponges.
254x150mm (123 x 123 DPI)

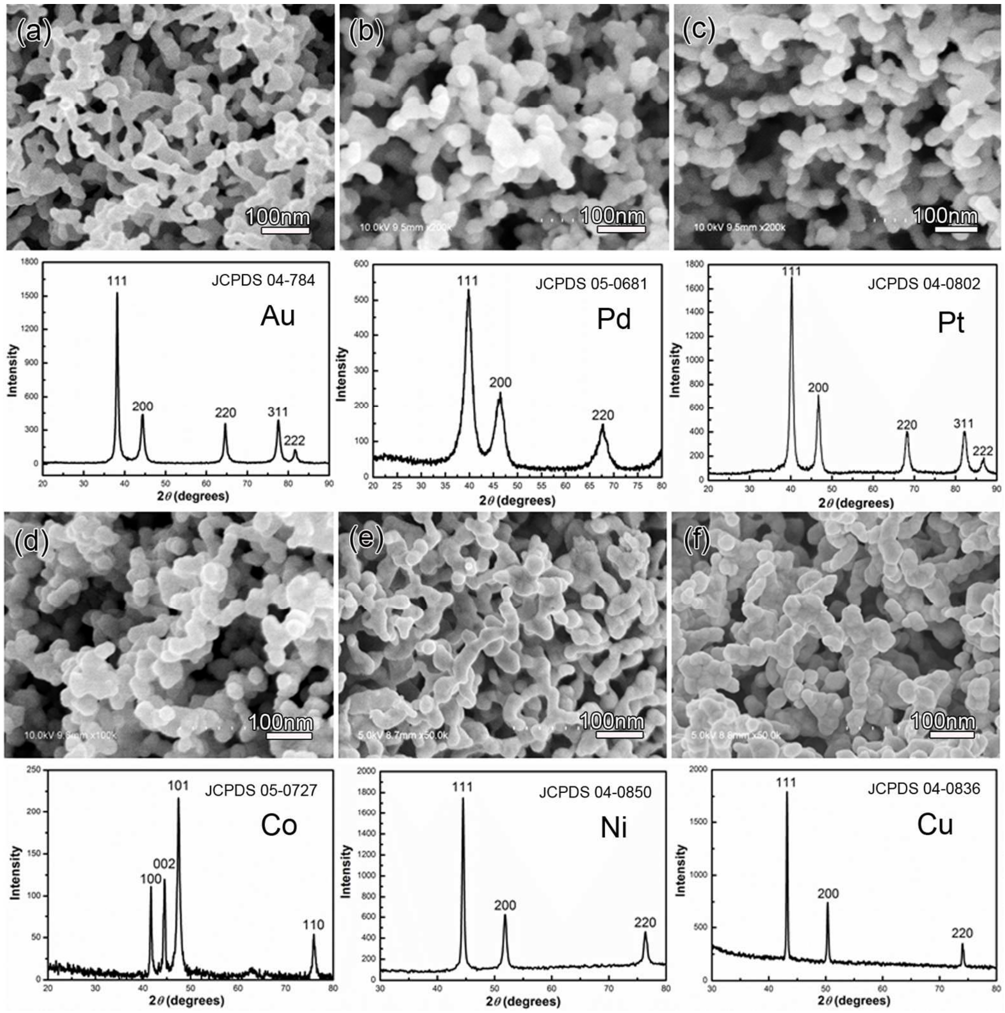

Fig. 2. SEM images of Au, Pd, Pt, Co, Ni, and Cu sponges (a-f, respectively). The corresponding XRD patterns are always below the images. The seven kinds of metals (including Ag) are close in the periodic table. Concentrations C of the different metal ion solutions are 24, 12, 12, 10, 10, and 15 mM for (a-f) respectively.
586x589mm (72 x 72 DPI)

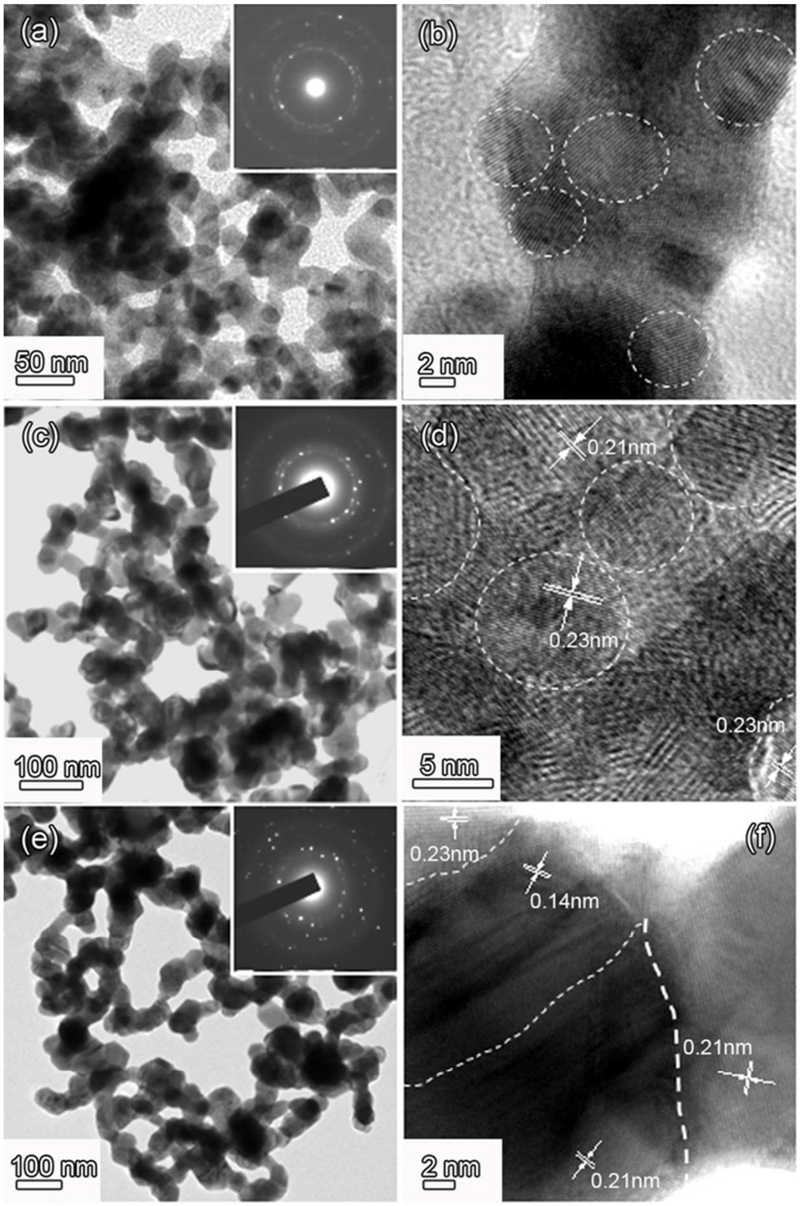

Fig. 3. TEM and HRTEM images of the Pd sponges obtained at different Tprep of 0 oC (a, b), r.t. (c, d), and 60 oC (e, f) while other conditions remained (CPd = 12 mM, Tf = 60 °C, and f = 80 rpm). The SAED patterns in the insets are recorded from a ligament in the corresponding samples.
126x190mm (150 x 150 DPI)

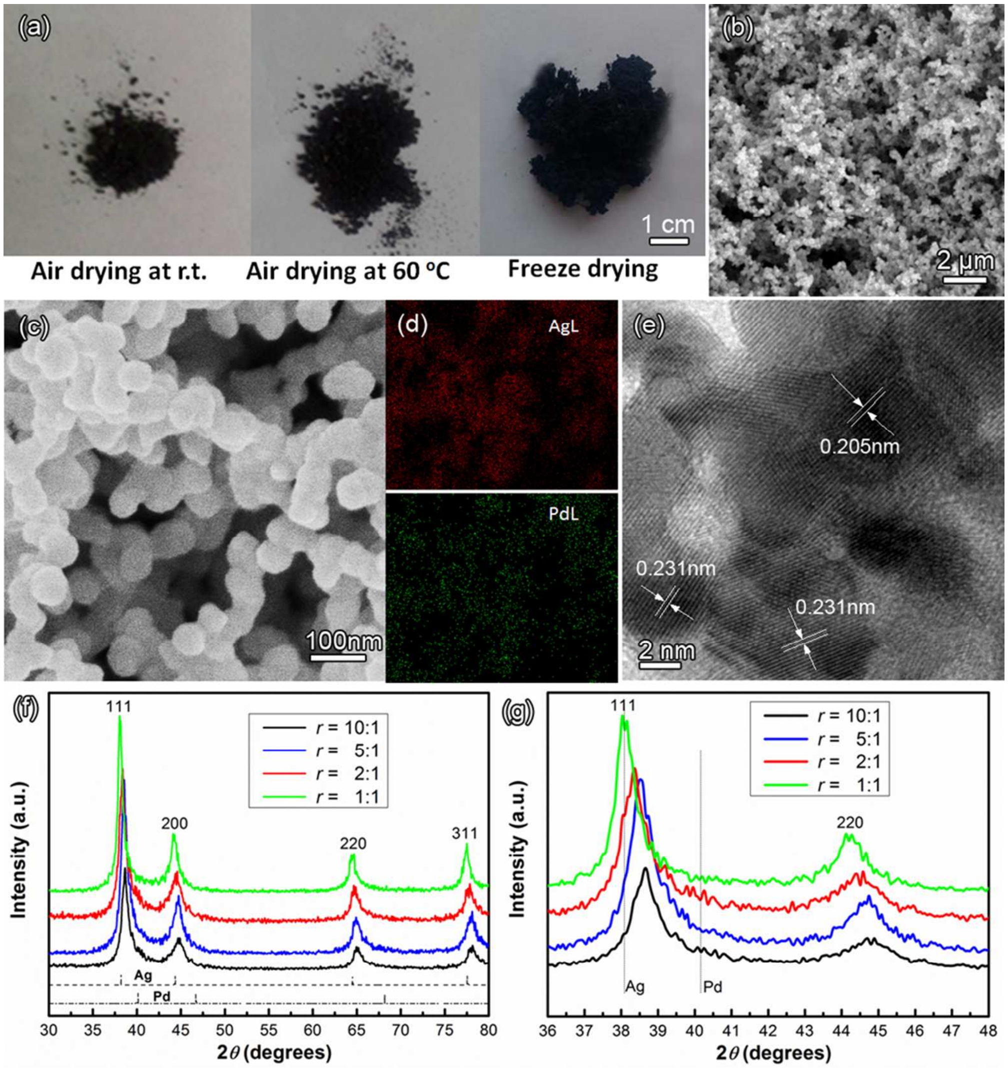

Fig. 4. Digital photographs (a) showing the Ag-Pd products from air drying at r.t. (on the left), air drying at 60 oC (middle), and freeze drying (right). SEM image (b, c), EDS-mapping (d), and HRTEM (e) images of the Ag0.5Pd0.5 alloy sponges. XRD patterns (f) of Ag-Pd sponges obtained with different molar ratios between PdCl4- and Ag+ ions. The (111) and (200) diffraction peaks are between the corresponding peaks of Ag and Pd (g), showing the samples are Ag-Pd alloy.
178x190mm (150 x 150 DPI)

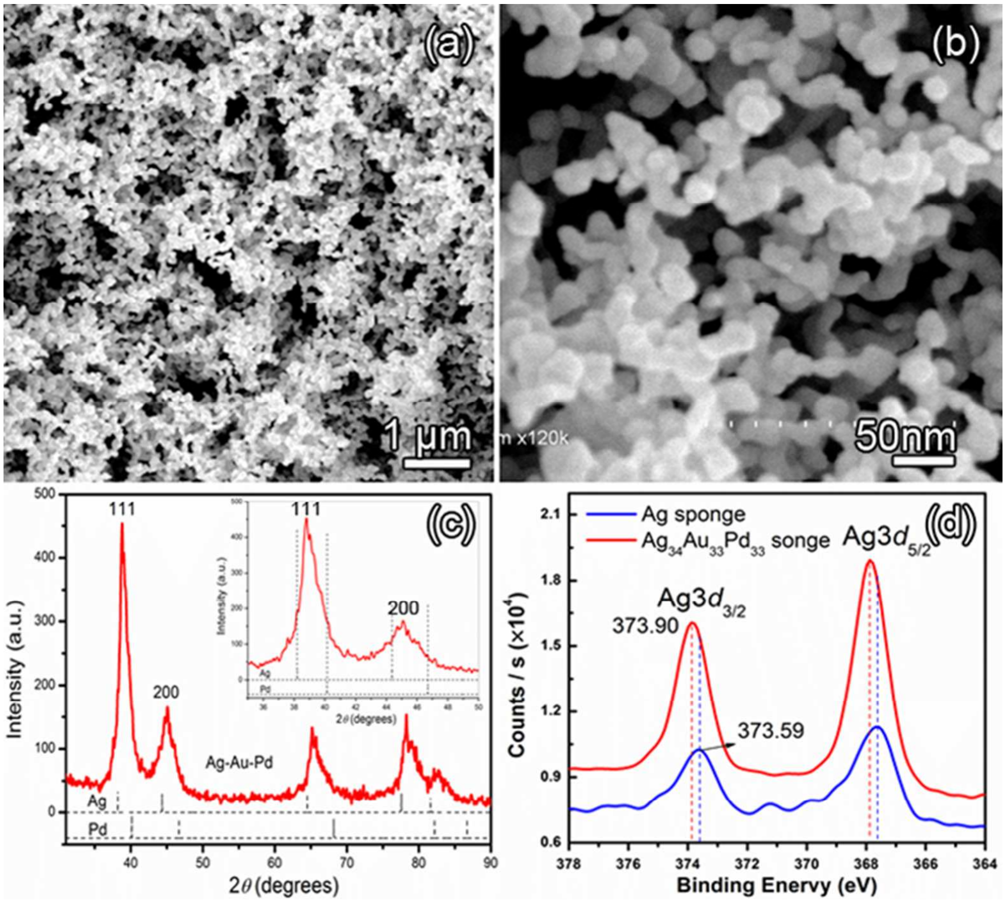

Fig. 5. SEM images (a, b), XRD pattern (c), and high resolution XPS spectrum of the Ag 3d peak (d) of the Ag34Au33Pd33 and the Ag sponges. The inset of c is a magnification of the (111) and (200) diffraction peaks.
213x190mm (88 x 88 DPI)

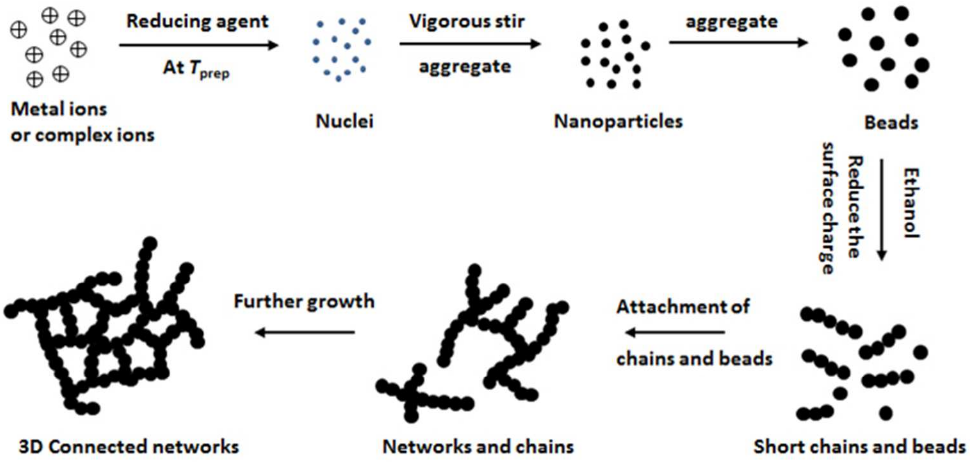

Scheme 1. Schematic illustration of the formation of nanosponges with 3D network-like nanostructure in ethanol-glycerol mixed solutions.
254x119mm (74 x 74 DPI)

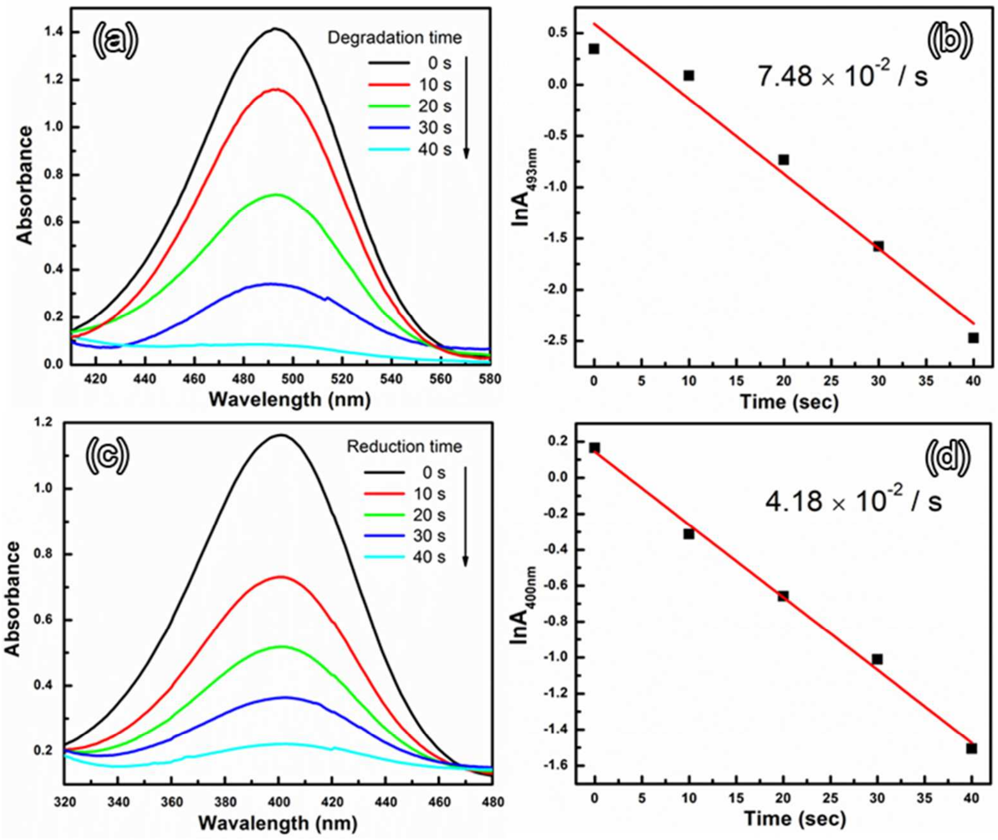

Fig. 6. UV-Vis absorption spectra for the decolourization of Congo red (a) and 4-NP reduction (c) in the presence of Ag34Au33Pd33 nanosponges. The plot of lnA versus time for the corresponding reactions (b and d). A is the absorption intensity.
227x190mm (93 x 93 DPI)

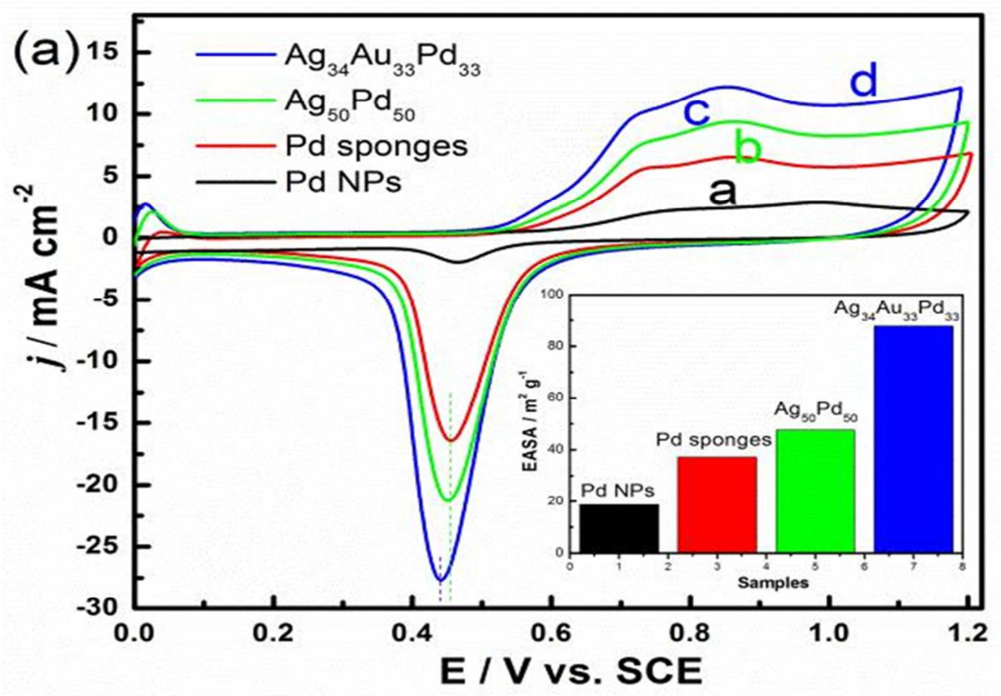

Fig. 7a CVs of Pd NPs, Pd, Ag50Pd50, and Ag34Au33Pd33 sponges modified GCs in a N2-saturated 0.5 M H2SO4 at 50 mV/s.
156x129mm (135 x 114 DPI)

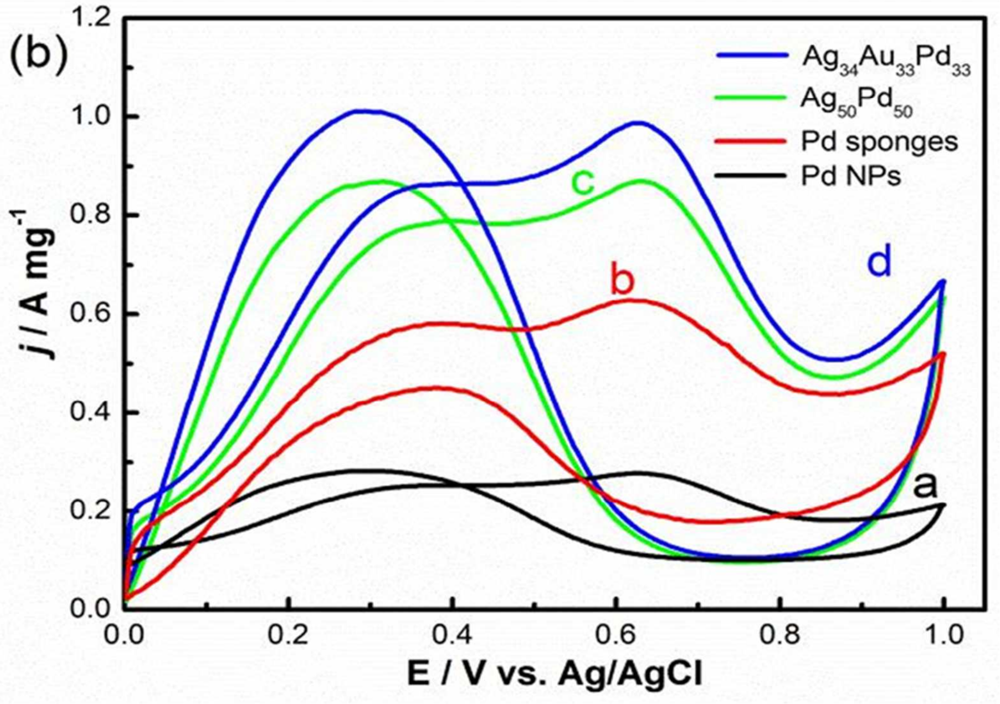

Fig. 7b CVs of Pd NPs, Pd, Ag50Pd50, and Ag34Au33Pd33 sponges modified GCs in a N2-saturated mixed solution containing 0.5 M H2SO4 and 0.5 M HCOOH at 50 mV/s.
169x129mm (121 x 112 DPI)

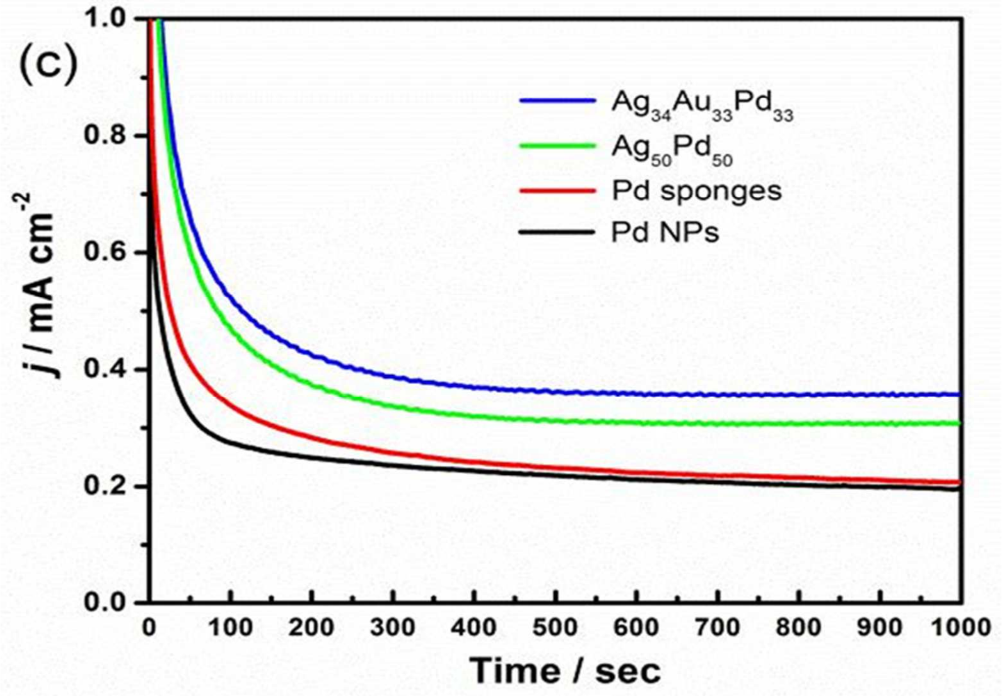

Fig. 7c Chronoamperometry responses were monitored at a fixed potential of 0.2 V versus SCE in the same mixed solution.
158x123mm (125 x 112 DPI)

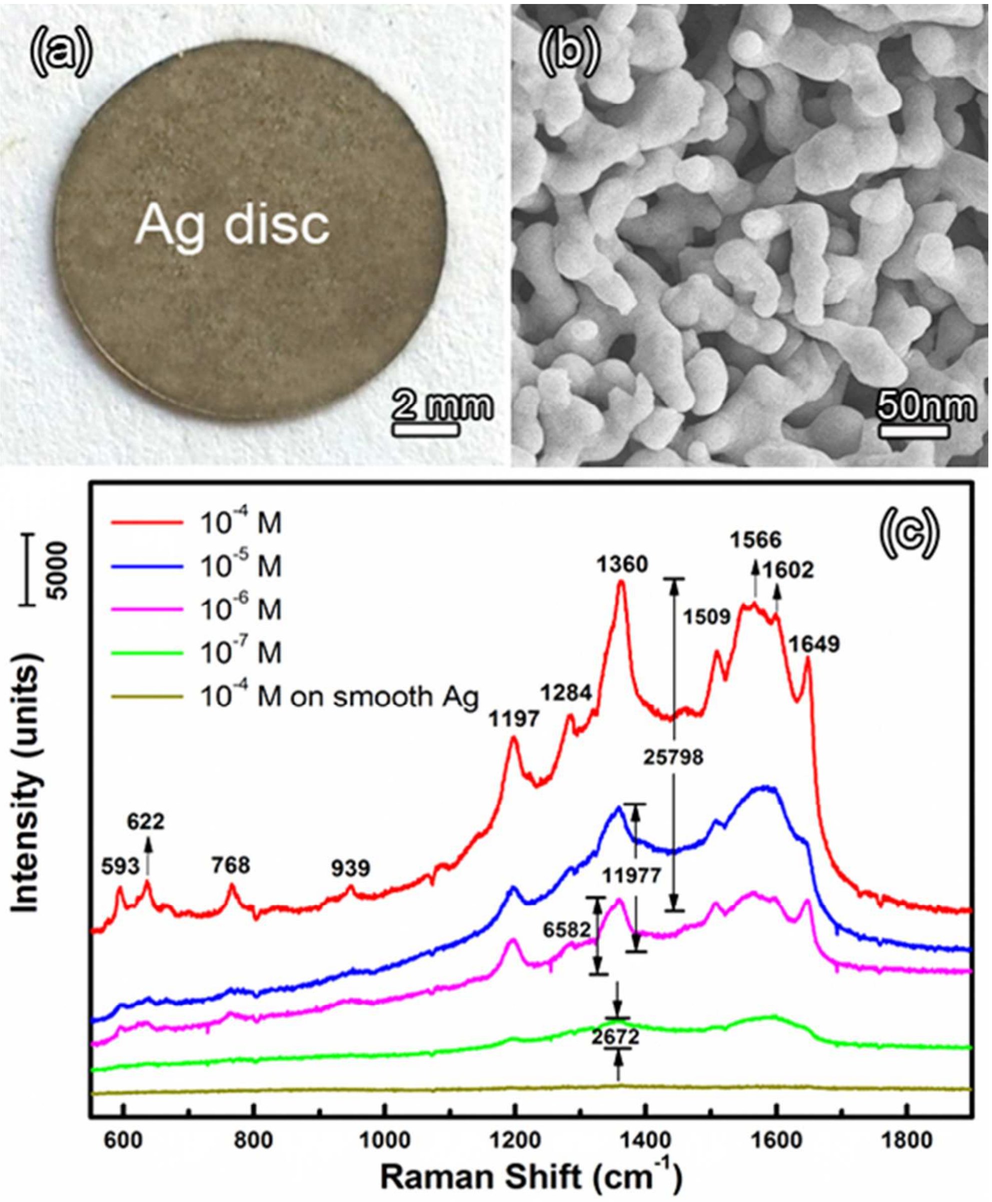

Fig. 8. Photograph of a disc made by applying a pressure of 10 kN on silver nanosponges. SEM image (b) showing a magnification of surface morphology of the disc. Raman spectra (c) of 10-4 M RhB on a smooth Ag sheet (light yellow curve), and RhB with different concentrations from 10-4 M to 10-7 M on the porous Ag disc.
157x190mm (97 x 97 DPI)